Linear and nonlinear optical and spin-optical response of gapped and proximitized graphene

Thomas Garm Pedersen*

Department of Physics and Nanotechnology, Aalborg University, DK-9220 Aalborg Øst, Denmark
and Center for Nanostructured Graphene (CNG), DK-9220 Aalborg Øst, Denmark

(Received 2 May 2018; revised manuscript received 26 September 2018; published 17 October 2018)

The properties of graphene can be significantly modified by interaction with a commensurate substrate. Via proximity effects, both band gaps and substantial spin-orbit coupling can be induced, opening a route to novel applications. In this work, we ask whether the linear and nonlinear optical response can be applied to probe the underlying symmetry of gapped and proximitized graphene. Answering in the affirmative, we show that, in particular, optical second-harmonic generation is a highly sensitive tool for characterization. Importantly, the spin-orbit sublattice symmetry is clearly revealed by the optical spectra. In addition, the topological phase of the materials is revealed via linear and nonlinear spin-optical effects.

DOI: 10.1103/PhysRevB.98.165425

I. INTRODUCTION

Graphene is an exceptional material in many respects but the lack of a band gap and sizable spin-orbit coupling is a serious obstacle for many applications in logic and spintronics devices [1,2]. A band gap can be induced in various ways including nanostructuring into nanoribbons [3,4] and antidot lattices [5,6]. Alternatively, interaction with a suitable substrate breaking the sublattice symmetry may open a gap in the spectrum [7,8]. This approach has the advantage of maintaining the high mobility of intact graphene. Importantly, however, certain substrates may also induce a substantial spin-orbit effect in graphene via proximity coupling [9–15]. Thus, gapped and proximitized graphene becomes feasible via such substrates. Recently, the existence of protected edge states was predicted for proximitized graphene nanoribbons due to the combination of spin-orbit coupling and confinement gap [16]. Thus, topological applications can be envisioned for graphene.

A substrate will impact all properties including mechanical, transport, thermal, magnetic, and optical. Among these, the optical response offers a unique possibility for contactless and noninvasive quantitative probing of the substrate-induced modifications. The opening of a gap is readily revealed in an absorption spectrum but, importantly, symmetry properties of the electronic states leave a mark on the optical selection rules. The linear optical response is relatively insensitive to symmetry properties in comparison to various nonlinear response functions. A striking example is offered by the linear and second-order response of gapped graphene with a staggered potential breaking sublattice symmetry. In this case, the linear response remains isotropic and the only significant modification is the opening of an absorption gap [17]. A pronounced modification of the linear magneto-optical response is observed in the presence of large-period modulations from, e.g., substrate-induced strain domains [18] or antidot lattices [19]. However, periods comparable to the characteristic magnetic length are required and a short-period modulation essentially simply adds a fundamental gap to the Landau-level gaps [20]. In contrast, the second-order nonlinear response in the dipole approximation is identically zero in the gapless case due to inversion symmetry. In the presence of a staggered potential, a nonvanishing response emerges having a pronounced sixfold rotation symmetry revealing the orientation of the material [21,22]. A similarly striking on-off effect is seen in the presence of a perpendicular bias applied to bilayer graphene [23,24]. Hence, significant information is revealed by characterization of the nonlinear response.

A few previous works have examined the suggestion that optical spectroscopy can reveal modifications to the Dirac spectrum of pristine graphene. In particular, optical signatures of topologically nontrivial phases have been studied. Gapped graphene with a simple staggered sublattice potential (mass term) is topologically trivial. However, adding additional interactions may render the topology nontrivial. Such added interactions may include k-dependent mass terms [25], intrinsic or extrinsic spin-orbit interaction [26,27], and the optical field itself [28] in the case of a Floquet topological insulator. As stressed in Ref. [29], optical spectroscopy probes excitations rather than the ground state. This, in fact, makes optics a highly sensitive probe of any added interaction, even in the topologically trivial regime. Hence, the topological nature of both linear and nonlinear optical effects can be demonstrated [29]. Moreover, optical interactions may be strongly enhanced by added interactions in both nontrivial [25] and trivial [26] phases. Mathematically, the topological nature of optical and transport response function is intimately tied to the Berry connection and curvature. We have previously demonstrated that these quantities play a crucial role via the generalized derivative (see also below) in both second-harmonic generation [22] and nonlinear photocurrents (shift currents) [30] in gapped graphene. Finally, single-band intraband second-order nonlinearities have been predicted in systems possessing a Berry curvature dipole [31,32]. It is therefore natural to extend this to the quantum interband regime.

*tgp@nano.aau.dk

In the present paper, the linear and second-order interband nonlinear optical response of modified graphene is computed using a general tight-binding parametrization. The envisioned modifications are assumed due to a commensurate substrate inducing a gap and spin-orbit coupling via the proximity effect. Effectively, the two atoms (A and B) in the unit cell are assumed to see different environments due to the substrate leading to sublattice-symmetry breaking. The difference in on-site potential opens a spectral gap. By allowing for a substrate-induced spin-orbit coupling between two A atoms that differs from the coupling between B atoms, a rich space of possible modifications emerges. We ignore Rashba coupling that could potentially lead to additional modifications. The linear optical conductivity and second-harmonic nonlinear susceptibility are used to gauge the proximity effects. Moreover, the linear and nonlinear spin-optical susceptibilities are demonstrated to clearly reveal the topological phase of the proximitized material. Crucially, optical and spin-optical second-harmonic generation is found to contain clear fingerprints of proximity effects. These signals are highly sensitive to the relative magnitude of A and B atom spin-orbit coupling as well as the crystal orientation. Hence, such responses provide a unique probe of the spin-orbit strength and symmetry.

II. THEORETICAL FRAMEWORK

Proximitized graphene is described by a tight-binding model [14–16] with couplings as illustrated in Fig. 1. Here, substrate-induced on-site energies for A and B atoms are denoted Δ and $-\Delta$, respectively, i.e., we take their average as the energy zero point. Also, the nearest-neighbor hopping is $-\gamma$ and a vanishing spin-orbit coupling between nearest neighbors is assumed. Finally, the substrate-induced spin-orbit coupling between second-nearest neighbors is $is_z\lambda_I\nu$ with $I = A, B$ distinguishing the sublattices, $s_z = \pm 1$ the spin, and $\nu = \pm 1$ depending on the rotation sense within a hexagon: $\nu = +1(-1)$ for clockwise (counterclockwise) orientation [14–16]. Substrate-induced strain is ignored and so the lattice constant $a = 2.46\,\text{Å}$ of pristine graphene is assumed.

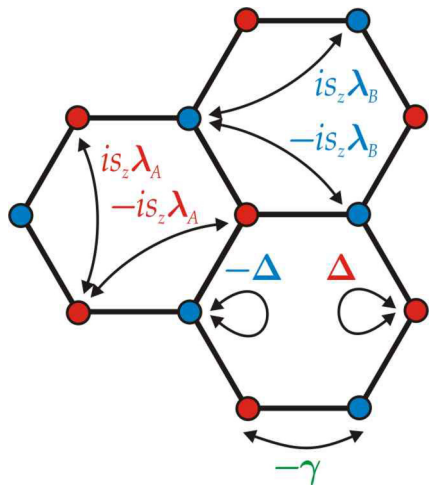

FIG. 1. Schematic of the tight-binding couplings modeling proximitized graphene with A and B atoms indicated by red and blue circles, respectively.

Placing the graphene sheet in the (x,y) plane, the two-band Hamiltonian for states with wave vector $\vec{k}$ resulting from these couplings is

$$\overleftrightarrow{H} = \begin{pmatrix} \Delta + s_z\lambda_A g & -\gamma f \\ -\gamma f^* & -\Delta - s_z\lambda_B g \end{pmatrix}, \tag{1}$$

with

$$\begin{aligned} f(\vec{k}) &= e^{ik_x a/\sqrt{3}} + 2e^{-ik_x a/2\sqrt{3}}\cos(k_y a/2), \\ g(\vec{k}) &= 2\{\sin(k_x a\sqrt{3}/2 + k_y a/2) - \sin(k_y a) \\ &\quad - \sin(k_x a\sqrt{3}/2 - k_y a/2)\}. \end{aligned} \tag{2}$$

This Hamiltonian is closely related to the Haldane [33] and Kane-Mele [34] models with the additional freedom of allowing for distinct sublattice spin-orbit couplings. Note that similarly to the Kane-Mele model but in contrast to the Haldane model, the Hamiltonian Eq. (1) respects time-reversal symmetry since the odd function $g(\vec{k})$ is multiplied by spin s_z. In pristine graphene, the gap closes at the Dirac points $\mathrm{K}: 2\pi(3^{-1/2}, 3^{-1})/a$ and $\mathrm{K}': 2\pi(3^{-1/2}, -3^{-1})/a$. In the proximitized case, $g(\mathrm{K}) = -3\sqrt{3}$ and $g(\mathrm{K}') = 3\sqrt{3}$, which eventually leads to gaps $E_{\mathrm{K}} = 2\Delta - s_z 3\sqrt{3}(\lambda_A + \lambda_B)$ and $E_{\mathrm{K}'} = 2\Delta + s_z 3\sqrt{3}(\lambda_A + \lambda_B)$. In the vicinity of the gaps, the bands follow gapped graphene dispersions, i.e., $E \approx \pm(E_{\mathrm{K}}^2/4 + \hbar^2 v_{\mathrm{K}}^2 k^2)^{1/2}$ and similarly for K′ with $\vec{k}$ measured relative to the respective Dirac point. The band velocities are

$$\begin{aligned} v_{\mathrm{K}}^2 &= v_F^2 - \frac{a^2}{\hbar^2}\left\{\frac{27}{8}(\lambda_A + \lambda_B)^2 - \frac{3\sqrt{3}}{4}s_z(\lambda_A + \lambda_B)\Delta\right\}, \\ v_{\mathrm{K}'}^2 &= v_F^2 - \frac{a^2}{\hbar^2}\left\{\frac{27}{8}(\lambda_A + \lambda_B)^2 + \frac{3\sqrt{3}}{4}s_z(\lambda_A + \lambda_B)\Delta\right\}, \end{aligned} \tag{3}$$

with $v_F = \sqrt{3}\gamma a/2\hbar$ the usual Fermi velocity of graphene.

In order to provide realistic estimates of proximity couplings Δ and $\lambda_{A,B}$, we turn to reported experimental band gaps and spin-orbit parameters. The band gaps of graphene on SiC and hexagonal boron nitride (hBN) are 260 and 31 meV, respectively [7,8]. Hence, a range of reasonable band gaps exists. Note, however, that in the case of SiC a large charge transfer leading to doping of graphene is observed [7]. The calculated spin-orbit coupling for graphene on transition-metal dichalcogenides is very small [14] but recent work for graphene on WS_2 shows that sulfur vacancies can substantially enhance the proximity effect leading to an induced spin-orbit coupling around 17 meV [9]. This number can be regarded as an estimate of presently achievable proximity-induced spin-orbit couplings. Obtaining simultaneously a substantial band gap and spin-orbit coupling is obviously challenging but optimal combinations might be realized by sandwiching graphene between different substrates such as, e.g., in SiC/graphene/WS_2 devices. For illustrational purposes, we focus on the extreme cases, i.e., uniform coupling $\lambda_A = \lambda_B$ and staggered coupling $\lambda_A = -\lambda_B$. Intermediate

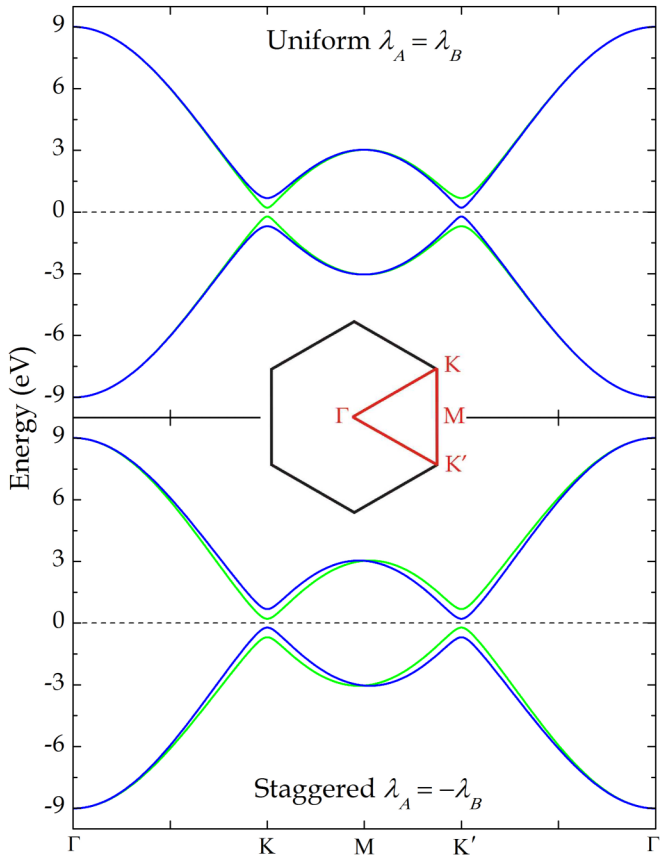

FIG. 2. Band structures of proximitized graphene in the uniform (top) and staggered (bottom) spin-orbit regimes. Green and blue lines show spin-up and -down bands, respectively.

cases follow by interpolation between these two extremes. In order to conform to realistic parameters, we take $\Delta = 50\,\text{meV}$ and $\lambda_A = 17\,\text{meV}$ in addition to $\gamma = 3\,\text{eV}$ characteristic of graphene, except for the case of hBN briefly considered below, for which $\Delta = 3.9\,\text{eV}$ and $\gamma = 2.33\,\text{eV}$ [22].

The condition for a topological nontrivial phase in the present model is $3\sqrt{3}(\lambda_A + \lambda_B)/2 > \Delta$ [33,34]. Hence, with the above parameters, proximitized graphene with uniform spin-orbit coupling is topologically nontrivial, whereas the staggered case is trivial. Also, proximitized hBN is obviously strongly trivial. The band structures of proximitized graphene with the above-mentioned parameters are shown in Fig. 2. In the uniform case, the band structure is electron-hole symmetric around 0 eV for each spin separately, whereas the bands in the staggered model are shifted vertically by the same k-dependent amount. The gaps at K and K′ are clearly visible in both cases but the symmetry is obviously different. Hence, in the uniform case, the gap magnitude for a specific spin differs but the midpoints remain at 0 eV. In contrast, in the staggered case, the gaps at K and K′ are both 2Δ but the midpoints are at $\pm 6\sqrt{3}\lambda_A$. These characteristic differences lead to significant fingerprints in the linear and nonlinear optical response as we now demonstrate.

The linear optical response is governed by the linear susceptibility tensor $\chi^{(1)}_{ij}$. Throughout, we ignore excitonic effects and therefore all results are computed in the independent-particle approximation. Moreover, a vanishing temperature is assumed and we restrict the analysis to intrinsic materials with the Fermi level in the fundamental energy gap. For a two-band, spin-orbit split material with a single valence band v and conduction band c per spin, one has [22]

$$\chi^{(1)}_{ij}(\omega) = \frac{e^2\hbar}{4\pi^2\varepsilon_0 m^2\omega} \times \sum_{s_z=\pm1}\int \frac{1}{E_{cv}}\left\{\frac{p^i_{cv}p^j_{vc}}{E_{cv}-\hbar\omega} - \frac{p^j_{cv}p^i_{vc}}{E_{cv}+\hbar\omega}\right\}d^2k, \tag{4}$$

where $E_{cv} = E_c(s_z,\vec{k}) - E_v(s_z,\vec{k})$ is the transition energy and $p^i_{cv} = \langle c, s_z, \vec{k}|p_i|v, s_z, \vec{k}\rangle$ is the momentum matrix element. The susceptibility is related to the conductivity via $\sigma = -i\omega\varepsilon_0\chi^{(1)}$, for which a convenient normalization is the graphene dc value $\sigma_0 = e^2/4\hbar$. Similarly, in the length gauge [35], the second-harmonic susceptibility $\chi^{(2)}_{ijk}$ is given by [22]

$$\chi^{(2)}_{ijk}(\omega) = \frac{3ie^3\hbar^2}{4\pi^2 m^2\varepsilon_0} \times \sum_{s_z=\pm1}\int \frac{p^i_{vc}\left(p^j_{cv}\right)_{;k_k}}{\left(E^2_{cv}-4(\hbar\omega)^2\right)\left(E^2_{cv}-(\hbar\omega)^2\right)}d^2k, \tag{5}$$

where $(O_{nm})_{;k} \equiv dO_{nm}/dk - iO_{nm}[\Omega_{nn} - \Omega_{mm}]$ denotes the generalized derivative expressed in terms of the Berry connection Ω [22]. In addition to these optical response functions, we also consider their spin-optical analogs

$$\chi^{(1S)}_{ij}(\omega) = \frac{e^2\hbar}{4\pi^2\varepsilon_0 m^2\omega}\sum_{s_z=\pm1}\int s_z\frac{1}{E_{cv}}\left\{\frac{p^i_{cv}p^j_{vc}}{E_{cv}-\hbar\omega} - \frac{p^j_{cv}p^i_{vc}}{E_{cv}+\hbar\omega}\right\}d^2k,$$

$$\chi^{(2S)}_{ijk}(\omega) = \frac{3ie^3\hbar^2}{4\pi^2 m^2\varepsilon_0}\sum_{s_z=\pm1}\int s_z\left\{\frac{p^i_{vc}\left(p^j_{cv}\right)_{;k_k}}{\left(E^2_{cv}-4(\hbar\omega)^2\right)\left(E^2_{cv}-(\hbar\omega)^2\right)}\right.$$
$$\left. - \frac{\left(2E^3_{cv} - 2E^2_{cv}\hbar\omega + E_{cv}(\hbar\omega)^2 + 2(\hbar\omega)^3\right)p^i_{vc}p^j_{cv}}{E^2_{cv}\left(E^2_{cv}-4(\hbar\omega)^2\right)\left(E^2_{cv}-(\hbar\omega)^2\right)(E_{cv}+\hbar\omega)(E_{cv}-2\hbar\omega)}\cdot\frac{dE_{cv}}{dk_k}\right\}d^2k. \tag{6}$$

The linear optical spin susceptibility yields the optical spin Hall conductivity $\sigma^{(S)}_{xy} = -i\omega\varepsilon_0\chi^{(1S)}_{xy}$ and, similarly, $\chi^{(2S)}_{ijk}$ describes the nonlinear optical spin susceptibility. A term similar to the second one in $\chi^{(2S)}_{ijk}$ could be added to Eq. (5)

but vanishes identically after summing over k and s_z due to time-reversal symmetry. However, in Eq. (6), time-reversal arguments cannot be applied due to the spin weight s_z and the more complicated expression results. By point-group and time-reversal symmetry, $\chi^{(1)}_{yy} = \chi^{(1)}_{xx}$ and $\chi^{(2)}_{xyy} = \chi^{(2)}_{yxy} = \chi^{(2)}_{yyx} = -\chi^{(2)}_{xxx}$, while all other elements of the optical susceptibilities vanish. In contrast, the nonvanishing elements of the optical spin susceptibilities are $\chi^{(1S)}_{xy} = -\chi^{(1S)}_{yx}$ and $\chi^{(2S)}_{yxx} = \chi^{(2S)}_{xyx} = \chi^{(2S)}_{xxy} = -\chi^{(2S)}_{yyy}$. These symmetries are summarized in Eq. (7), in which dots designate equal magnitudes and open vs filled dots indicate a relative sign difference.

$$\begin{array}{cc|cc|ccccc|ccccc} & & \multicolumn{2}{c|}{\sigma} & \multicolumn{2}{c|}{\sigma^{(S)}} & & \multicolumn{4}{c|}{\chi^{(2)}} & & \multicolumn{4}{c}{\chi^{(2S)}} \\ & & x & y & x & y & & xx & xy & yx & yy & & xx & xy & yx & yy \\ x & & \bullet & 0 & x & 0 & x & \bullet & 0 & 0 & \circ & x & 0 & \circ & \circ & 0 \\ y & & 0 & \bullet & y & \circ & y & 0 & \circ & \circ & 0 & y & \circ & 0 & 0 & \bullet \end{array} \tag{7}$$

We evaluate these response functions by numerical sampling of the Brillouin zone applying analytical expressions for the energies and momenta using at least $9 \times 10^6 k$ points. The k derivatives in Eqs. (5) and (6) are computed from a finite-difference approximation. Hence, for numerical purposes, it is convenient to apply an equivalent rectangular Brillouin zone instead of the hexagonal one shown in Fig. 2. Also, an imaginary part $i\Gamma$ with $\hbar\Gamma = 10\,\mathrm{meV}$ is added to the frequency ω in Eqs. (4)–(6) to include line broadening.

III. LINEAR AND NONLINEAR OPTICAL RESPONSE

The real part of the linear optical conductivity is illustrated in Fig. 3 for the uniform and staggered cases. In addition to the numerical tight-binding results, we compare with the analytical Dirac approximation [17], in which the gapped graphene dispersion $E_{cv} = (E^2_{\mathrm{K},\mathrm{K}'} + 4\hbar^2 v^2_{\mathrm{K},\mathrm{K}'} k^2)^{1/2}$ is adopted and the momenta and energy corrections are expanded to lowest order at the Dirac points. For the purely optical response functions considered, we find

$$\sigma_{xx}(\omega) = \frac{i\sigma_0}{\pi}\left\{\frac{|E_\mathrm{K}|}{\hbar\omega} - \left(1 + \frac{E_\mathrm{K}^2}{(\hbar\omega)^2}\right)\tanh^{-1}\left(\frac{\hbar\omega}{|E_\mathrm{K}|}\right)\right\} + (\mathrm{K} \to \mathrm{K}'), \tag{8}$$

$$\chi^{(2)}_{xxx}(\omega) = \frac{e^3 a|E_\mathrm{K}|}{16\sqrt{3}\pi\varepsilon_0(\hbar\omega)^3}\left\{2\tanh^{-1}\left(\frac{\hbar\omega}{E_\mathrm{K}}\right) - \tanh^{-1}\left(\frac{2\hbar\omega}{E_\mathrm{K}}\right)\right\} + (\mathrm{K} \to \mathrm{K}'). \tag{9}$$

The spin-orbit sublattice symmetry, i.e., uniform vs staggered, is clearly revealed by the presence of a double- vs single-gapped spectrum. In the linear response shown in Fig. 3, two pronounced steps appear in the absorption spectrum of the uniform model, both in tight-binding and Dirac approaches. Using the above-mentioned parameters, the two gaps in the uniform case are at 77 and 277 meV, whereas the single gap found in the staggered case is located at 100 meV. The high-energy part of the spectrum is insensitive to the spin-orbit symmetry. Hence, the primary diagnostic using the linear response is based on the gap structure. This is reminiscent of the impact of Rashba spin-orbit coupling in graphene [27].

The second-harmonic susceptibility shown in Fig. 4 is very sensitive to the symmetry in the entire frequency range characterized by a large response. In addition to resonances at the gaps E_K and $E_{\mathrm{K}'}$, so-called 2ω resonances at $E_\mathrm{K}/2$ and $E_{\mathrm{K}'}/2$ are observed. In the uniform case, the two lowest resonances are at 38 and 77 meV and a second pair at twice these energies is observed. Conversely, only two features at 50 and 100 meV are found in the staggered case. The magnitude of the response is quite high as a consequence of the low photon energy at resonance. This can be contrasted with the case of proximitized hexagonal boron nitride shown in Fig. 5. Here, the quasiparticle band gap 2Δ of pristine

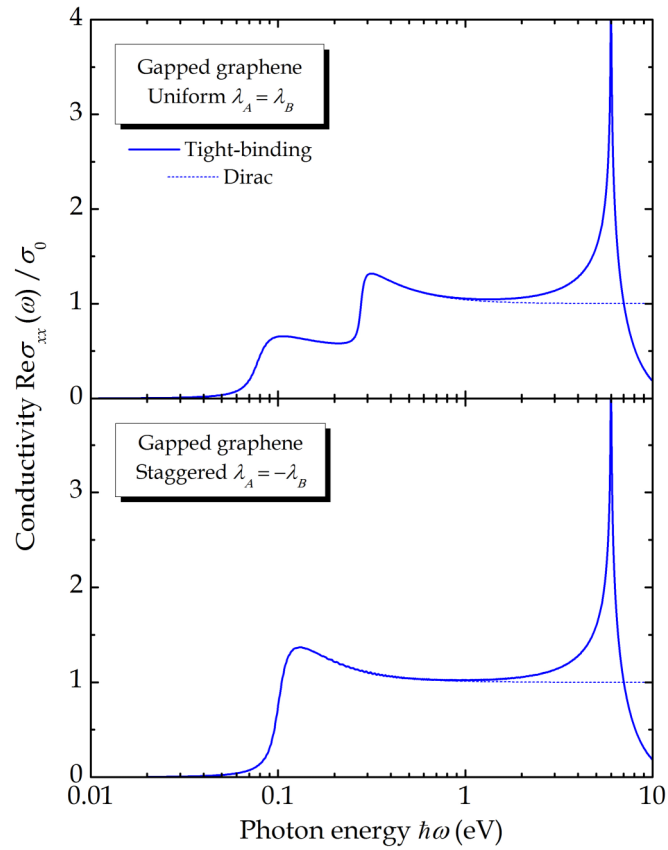

FIG. 3. Linear optical conductivity in units of the graphene dc value σ_0. The double- and single-gap structure is revealed in the uniform (upper panel) and staggered (lower panel) cases, respectively. This characteristic is visible in both tight-binding (full lines) and Dirac (dashed lines) models.

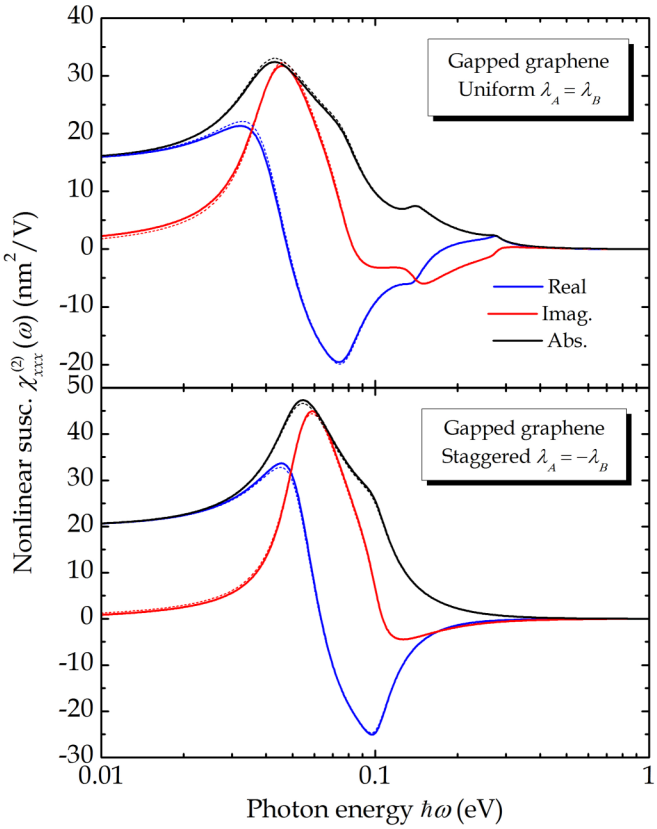

FIG. 4. Second-harmonic susceptibility of gapped graphene with uniform (upper panel) and staggered (lower panel) spin-orbit sublattice symmetry. Full and dashed lines show tight-binding and Dirac results, respectively.

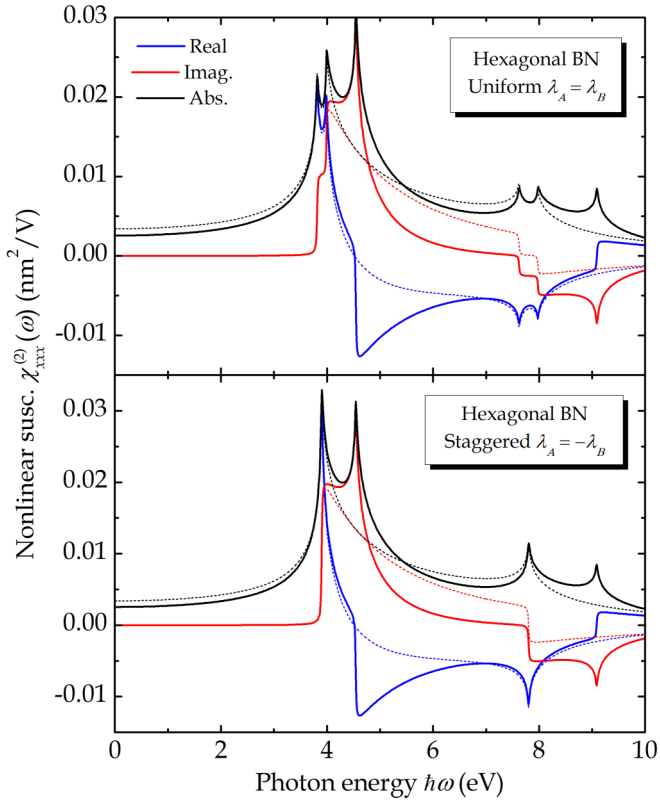

FIG. 5. Same as Fig. 4 but for proximitized hBN.

hBN is at 7.8 eV and, hence, the lowest 2ω resonance is near 3.9 eV. As a consequence, the signal at resonance is considerably lower than that of gapped graphene in Fig. 4. In the staggered case, the nonlinear response of proximitized hBN is identical to that of pristine hBN [22]. The uniform spin-orbit coupled case in the upper panel of Fig. 5, however, is significantly modified, revealing additional splittings. As a consequence, second-harmonic generation is an extremely sensitive probe of spin-orbit sublattice symmetry. We note that other mechanisms of second-harmonic generation in graphene have been identified: current injection [36], valley polarization via a valley-dependent Fermi level [37,38], and nonlocal excitation beyond the electric-dipole limit [39]. The first two are nonequilibrium phenomena that require biasing or optical pumping. In addition, nonlocal excitation only takes place with pumping at oblique angles of incidence whereas a proximity-induced second harmonic would appear at normal incidence also. Hence, there are several characteristic signatures that distinguish the mechanism discussed here.

The Dirac approximation shown as dashed lines in Figs. 3–5 is excellent in the energy range dominated by the Dirac points K and K'. It completely fails, however, to capture the van Hove contributions corresponding to the M points of the Brillouin zone. This singularity gives rise to the resonance around 6 eV in the linear response in Fig. 3. Similarly, the peaks in the nonlinear response at approximately 4.5 and 9 eV in proximitized hBN shown in Fig. 5 are missing in the Dirac result for the same reason. The second-harmonic response of proximitized graphene (Fig. 4) is completely dominated by the Dirac points and, therefore, very accurately described by the Dirac model.

IV. LINEAR AND NONLINEAR SPIN-OPTICAL RESPONSE

In this section, we turn to the linear and nonlinear contributions to the spin-optical response given by Eqs. (6). Characteristically, all purely optical response tensor elements containing an odd number of y components vanish identically due to inversion and time-reversal symmetries. This may be viewed as an effect of canceling valley contributions. For instance, the Hall conductivity of the K valley $\sigma^{(1,\mathrm{K})}_{xy}$ is not vanishing but, in fact, of the same order as the diagonal conductivity. However, for the K' valley one has $\sigma^{(1,\mathrm{K}')}_{xy} = -\sigma^{(1,\mathrm{K})}_{xy}$ and, consequently, the total Hall response vanishes. A similar argument applies to the nonlinear response such as $\chi^{(2)}_{xyx}$. In contrast, when the different contributions to the response are weighted by the spin s_z as in Eqs. (6), the valley contributions are weighted by opposite sign factors leading to finite linear off-diagonal response $\sigma^{(S)}_{xy}$ but a vanishing diagonal one $\sigma^{(S)}_{xx}$ as illustrated in Eq. (7). A similar interchange between finite and vanishing tensor elements is found in the nonlinear case. In the Dirac approximation, one finds

$$\sigma^{(S)}_{xy}(\omega) = -\frac{e^2}{\hbar}\left\{\frac{E_\mathrm{K}}{\hbar\omega}\tanh^{-1}\left(\frac{\hbar\omega}{|E_\mathrm{K}|}\right) - (\mathrm{K}\to\mathrm{K}')\right\}, \quad (10)$$

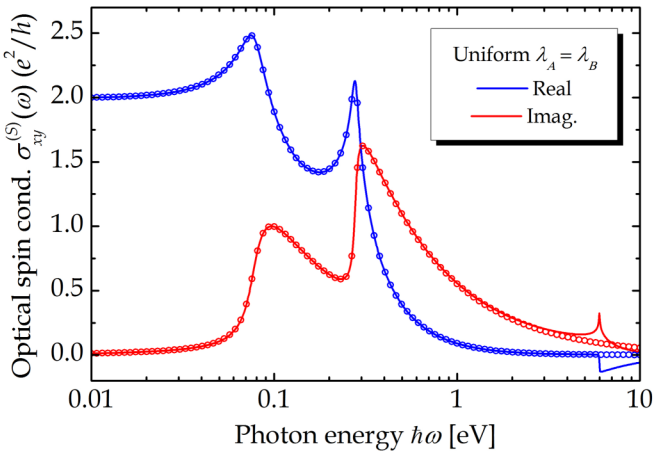

FIG. 6. Optical spin Hall conductivity of gapped graphene with uniform sublattice spin-orbit symmetry. The corresponding response in the staggered case vanishes. Dots are Dirac approximation results.

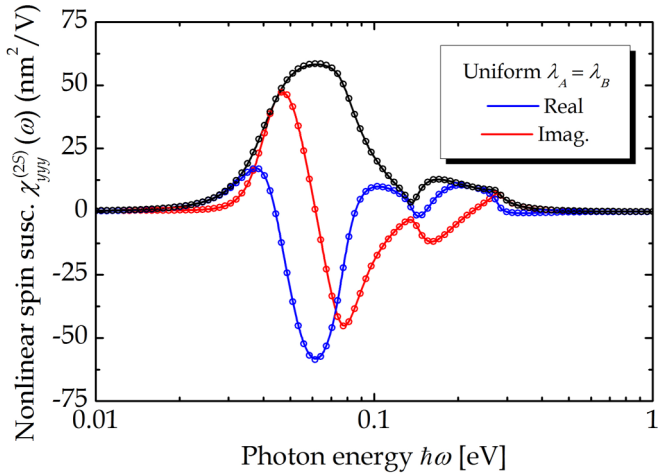

FIG. 7. Nonlinear optical spin susceptibility of gapped graphene with uniform sublattice spin-orbit symmetry. Full lines are tight-binding and dots are Dirac approximation results.

$$\chi^{(2S)}_{yyy}(\omega) = \frac{ie^3a}{2\sqrt{3}\pi\varepsilon_0(\hbar\omega)^2} \times \left\{-2\left(5+\frac{6E_{\rm K}^2}{(\hbar\omega)^2}-\frac{3E_{\rm K}^4}{(\hbar\omega)^4}\right)\tanh^{-1}\left(\frac{\hbar\omega}{|E_{\rm K}|}\right) + \left(8+\frac{6E_{\rm K}^2}{(\hbar\omega)^2}-\frac{3E_{\rm K}^4}{(\hbar\omega)^4}\right)\tanh^{-1}\left(\frac{2\hbar\omega}{|E_{\rm K}|}\right) + \frac{6|E_{\rm K}|}{\hbar\omega}\right\} - ({\rm K}\to{\rm K}'). \quad (11)$$

Here, by convention, spin-up band gaps should be applied. The static limit of the optical spin Hall conductivity Eq. (10) is

$$\sigma^{(S)}_{xy}(0) = -\frac{e^2}{\hbar}({\rm sgn}E_{\rm K} - {\rm sgn}E_{\rm K'}). \quad (12)$$

This result is the expected TKNN (Thouless-Kohmoto-Nightingale-Nijs) formula [40] for the static spin Hall effect in terms of Chern numbers ${\rm sgn}E_{\rm K}$ and $-{\rm sgn}E_{\rm K'}$ for the two valleys, where the sign difference is due to the spin weight. Thus, in the topologically trivial phase, for which $E_{\rm K}, E_{\rm K'} > 0$, the static spin Hall conductivity vanishes. The dynamical one $\sigma^{(S)}_{xy}(\omega > 0)$, however, remains finite as long as $E_{\rm K} \neq E_{\rm K'}$. Note the characteristic feature of both spin-optical response functions Eqs. (10) and (11) that the *difference* between valley contributions appears, in contrast to the regular optical response Eqs. (8) and (9), for which the contributions are added.

In Figs. 6 and 7, we show the numerical tight-binding results for both linear and nonlinear spin-optical response functions. In the linear case, the combined Chern number of 2 is readily identified as the dc limit of the response in both full and Dirac results. In fact, the Dirac approximation Eq. (10) is surprisingly accurate in the entire spectral range with the exception of the small M-point contribution near 6 eV. The spin-optical response is clearly very sensitive to spin-orbit symmetry but, unfortunately, less easily observed experimentally in comparison with the normal response. Thus, the usual optical Hall conductivity leads to effects such as Faraday rotation of the polarization state, which is easily detected. In contrast, spin-optical effects lead to spatial separation of spins and spin-sensitive probes are required for the detection. In traditional III-V semiconductors, spatially resolved optical Kerr rotation [41] and electroluminescence [42] have successfully detected spin Hall effects. Similarly, spin transport measurements have revealed spin-orbit-induced spin currents in graphene [43]. Thus, both optical and transport probes can be imagined to provide experimental fingerprints of the nonlinear response in Fig. 7. The magnitude of the nonlinear spin-optical susceptibility $\chi^{(2S)}_{yyy}$ is of the same magnitude as the optical response $\chi^{(2)}_{xxx}$ as demonstrated by comparing Figs. (4) and (7). Moreover, the symmetry properties of the two nonlinear susceptibilities are exactly opposite. Thus, the *yyy* component is finite only in the spin-optical case. This fact could potentially provide a clear fingerprint for detection.

V. SUMMARY

Summarizing, we have investigated the linear and second-order nonlinear optical response of graphene proximitized by a commensurate substrate. The bipartite sublattice symmetry is broken both by distinct on-site interactions and by substrate-induced spin-orbit couplings. In particular, we consider spin-orbit interactions for the two sublattices of either equal (uniform) or opposite (staggered) magnitudes. The different electronic spectra of these models lead to significant fingerprints in the optical response. In the linear response, different spin-orbit sublattice symmetries manifest themselves in the absorption gap. Hence, in the uniform case, a valley-dependent band gap leads to a double-gapped optical spectrum, whereas the staggered case is characterized by a single gap. The second-harmonic optical response is significant only in the spectral vicinity of the substrate-induced band gap and, hence, is highly indicative of proximity effects. Finally, the linear and nonlinear spin-optical response functions are particularly sensitive to spin-orbit sublattice symmetry and, in fact, vanish identically in the staggered case.

ACKNOWLEDGMENTS

Numerous useful discussions with A. Taghizadeh are gratefully acknowledged. This work is financially supported by the Center for Nanostructured Graphene (CNG) and the QUSCOPE center. CNG is sponsored by the Danish National Research Foundation, Project No. DNRF103 and QUSCOPE is sponsored by the Villum foundation.

[1] F. Schwierz, Nat. Nanotechnol. **5**, 487 (2010).
[2] W. Han, R. K. Kawakami, M. Gmitra, and J. Fabian, Nat. Nanotechnol. **9**, 794 (2014).
[3] Y.-W. Son, M. L. Cohen, and S. G. Louie, Phys. Rev. Lett. **97**, 216803 (2006).
[4] X. Li, X. Wang, L. Zhang, S. Lee, and H. Dai, Science **319**, 1229 (2008).
[5] T. G. Pedersen, C. Flindt, J. Pedersen, N. A. Mortensen, A.-P. Jauho, and K. Pedersen, Phys. Rev. Lett. **100**, 136804 (2008).
[6] R. Petersen, T. G. Pedersen, and A.-P. Jauho, ACS Nano **5**, 523 (2011).
[7] S. Y. Zhou, G. H. Gweon, A. V. Fedorov, P. N. First, W. A. De Heer, D. H. Lee, F. Guinea, A. H. Castro Neto, and A. Lanzara, Nat. Mater. **6**, 770 (2007).
[8] C. R. Woods, L. Britnell, A. Eckmann, R. S. Ma, J. C. Lu, H. M. Guo, X. Lin, G. L. Yu, Y. Cao, R. V. Gorbachev, A. V. Kretinin, J. Park, L. A. Ponomarenko, M. I. Katsnelson, Yu. N. Gornostyrev, K. Watanabe, T. Taniguchi, C. Casiraghi, H.-J. Gao, A. K. Geim, and K. S. Novoselov, Nat. Phys. **10**, 451 (2014).
[9] A. Avsar, J. Y. Tan, T. Taychatanapat, J. Balakrishnan, G. K. W. Koon, Y. Yeo, J. Lahiri, A. Carvalho, A. S. Rodin, E. C. T. O'Farrell, G. Eda, A. H. Castro Neto, and B. Özyilmaz, Nat. Commun. **5**, 4875 (2014).
[10] K.-H. Jin and S.-H. Jhi, Phys. Rev. B **87**, 075442 (2013).
[11] M. Gmitra and J. Fabian, Phys. Rev. B **92**, 155403 (2015).
[12] Z. Lin, W. Qin, J. Zeng, W. Chen, P. Cui, J.-H. Cho, Z. Qiao, and Z. Zhang, Nano Lett. **17**, 4013 (2017).
[13] S. Omar and B. J. van Wees, Phys. Rev. B **97**, 045414 (2018).
[14] M. Gmitra, D. Kochan, P. Högl, and J. Fabian, Phys. Rev. B **93**, 155104 (2016).
[15] D. Kochan, S. Irmer, and J. Fabian, Phys. Rev. B **95**, 165415 (2017).
[16] T. Frank, P. Högl, M. Gmitra, D. Kochan, and J. Fabian, Phys. Rev. Lett. **120**, 156402 (2018).
[17] T. G. Pedersen, A.-P. Jauho, and K. Pedersen, Phys. Rev. B **79**, 113406 (2009).
[18] L. A. Chizhova, J. Burgdörfer, and F. Libisch, Phys. Rev. B **92**, 125411 (2015).
[19] J. G. Pedersen and T. G. Pedersen, Phys. Rev. B **87**, 235404 (2013).
[20] J. G. Pedersen and T. G. Pedersen, Phys. Rev. B **84**, 115424 (2011).
[21] V. A. Margulis, E. E. Muryumin, and E. A. Gaiduk, J. Phys.: Condens. Matter **25**, 195302 (2013).
[22] T. G. Pedersen, Phys. Rev. B **92**, 235432 (2015).
[23] S. Wu, L. Mao, A. M. Jones, W. Yao, C. Zhang, and X. Xu, Nano Lett. **12**, 2032 (2012).
[24] S. J. Brun and T. G. Pedersen, Phys. Rev. B **91**, 205405 (2015).
[25] N. M. R. Peres and J. E. Santos, J. Phys.: Condens. Matter **25**, 305801 (2013).
[26] H. Rostami and R. Asgari, Phys. Rev. B **89**, 115413 (2014).
[27] W. Wang, C. Zhang, and Z. Ma, J. Phys.: Condens. Matter **24**, 035303 (2012).
[28] H. Dehghani and A. Mitra, Phys. Rev. B **92**, 165111 (2015).
[29] T. Morimoto and N. Nagaosa, Sci. Adv. **2**, e1501524 (2016).
[30] F. Hipolito, T. G. Pedersen, and V. M. Pereira, Phys. Rev. B **94**, 045434 (2016).
[31] I. Sodemann and L. Fu, Phys. Rev. Lett. **115**, 216806 (2015).
[32] Y. Zhang, Y. Sun, and B. Yan, Phys. Rev. B **97**, 041101(2018).
[33] F. D. M. Haldane, Phys. Rev. Lett. **61**, 2015 (1988).
[34] C. L. Kane and E. J. Mele, Phys. Rev. Lett. **95**, 146802 (2005).
[35] A. Taghizadeh, F. Hipolito, and T. G. Pedersen, Phys. Rev. B **96**, 195413 (2017).
[36] Y. Q. An, J. E. Rowe, D. B. Dougherty, J. U. Lee, and A. C. Diebold, Phys. Rev. B **89**, 115310 (2014).
[37] L. E. Golub and S. A. Tarasenko, Phys. Rev. B **90**, 201402 (2014).
[38] F. Hipolito and V. M. Pereira, 2D Mater. **4**, 021027 (2017).
[39] Y. Wang, M. Tokman, and A. Belyanin, Phys. Rev. B **94**, 195442 (2016).
[40] D. J. Thouless, M. Kohmoto, M. P. Nightingale, and M. den Nijs, Phys. Rev. Lett. **49**, 405 (1982).
[41] Y. K. Kato, R. C. Myers, A. C. Gossard, and D. D. Awschalom, Science **306**, 1910 (2004).
[42] J. Wunderlich, B. Kaestner, J. Sinova, and T. Jungwirth, Phys. Rev. Lett. **94**, 047204 (2005).
[43] J. Balakrishnan, G. K. W. Koon, A. Avsar, Y. Ho, J. H. Lee, M. Jaiswal, S. Baeck, J. Ahn, A. Ferreira, M. A. Cazalilla, A. H. Castro Neto, and B. Özyilmaz, Nat. Commun. **5**, 4748 (2014).